Mesoscopic Model of Extrusion during Solvent-Free Li-Ion Battery Electrode Manufacturing

Brayan Paredes-Goyes,[a,b] Franco M. Zanotto,[a,b] Victor Boudeville,[a,b] Sylvie Grugeon,[a,b] Loic Dupont,[a,b,c,d] and Alejandro A. Franco*[a,b,c,e]

[a]   Dr. B. Paredes-Goyes, V. Boudeville, Dr. F. M. Zanotto, Prof. Dr. L. Dupont, Dr. S. Grugeon, Prof. Dr. A. A. Franco
        Laboratoire de Réactivité et Chimie des Solides (LRCS), UMR CNRS 7314
        Université de Picardie Jules Verne, Hub de l'Energie
        15 rue Baudelocque, 80039 Amiens Cedex, France
        E-mail: alejandro.franco@u-picardie.fr

[b]   Dr. B. Paredes-Goyes, V. Boudeville, Dr. F. M. Zanotto, Prof. Dr. L. Dupont, Dr. S. Grugeon, Prof. Dr. A. A. Franco
        Réseau sur le Stockage Electrochimique de l'Energie (RS2E), FR CNRS 3459
        Hub de l'Energie
        15 rue Baudelocque, 80039 Amiens Cedex, France

[c]   Prof. Dr. A. A. Franco
        ALISTORE-European Research Institute, FR CNRS 3104
        Hub de l'Energie
        15 rue Baudelocque, 80039 Amiens Cedex, France

[d]   Prof. Dr. L. Dupont
        Plateforme de Microscopies Electroniques de l'UPJV
        Hub de l'Energie
        15 rue Baudelocque, 80039 Amiens Cedex, France

[e]   Prof. Dr. A. A. Franco
        Institut Universitaire de France
        103 Boulevard Saint Michel, 75005 Paris, France

Abstract: Solvent-free (SF) manufacturing of Lithium-ion battery (LIB) electrodes is safer and more environmentally friendly than the traditional slurry casting approach. However, as a young technique, SF manufacturing is under development of its pathways and operation conditions. In different SF processes reported in literature, extrusion is a common step. A detailed model of this process would be extremely computationally demanding. This work proposes a novel simplified discrete element model at the mesoscopic scale for the extrusion during SF manufacturing of LIB electrodes. In addition to active material particles, we consider fluid-like solid particles to approximate the molten polymer and the carbon additive phases. The formulation and other process parameters are taken from our experimental facility that uses extrusion to fabricate filaments for 3D printing of LIB cells. The simulations are carried out in a conical twin-screw extruder. Our approach allows to obtain representative electrode microstructures after extrusion, where electrical conductivity, ionic effective diffusivity, tortuosity factor and porosity are calculated. The model is a proof of concept that is employed to investigate the influence of the extruder speed and the cohesion level on the resulting electrode properties.

Introduction

The rise of the production of Lithium-ion batteries (LIBs) calls for a global improvement of the electrode manufacturing process. At present, slurry casting is the standard technique. The solvent-free (SF) approach appears as a prominent alternative as it avoids the use of toxic solvents and decreases the environmental impact.[1][2] Four different processes have been employed in the SF approach: hot pressing, spray deposition, dry process by melting extrusion (MeltE) and 3D printing by material extrusion (3DP).[1]

The MeltE approach in the SF porous electrode manufacturing has been proposed recently by a few research groups.[3][4][5] Although the stages themselves may vary, the main steps of this process typically adhere to a similar pathway (Fig 1a). Initially all the raw materials are in solid phase and include active material (AM), carbon additive (CA), permanent binder and sacrificial binder. The latter allows to create the porosity in the electrode and also improves the extrusion processability by increasing the polymer content. Extrusion allows the melting of the binders and facilitates the mixing of all formulation components under high shear rates. This process can be performed in twin-screw extruders (TSE) or in internal mixers. The latter are typically employed only at an academic scale to minimize the use of raw materials. [1] After going through the extruder outlet, the resulting paste solidifies, which allows for subsequent calendering and partial debinding steps. This is necessary for attaining the desired final electrode microstructure.

Material extrusion is one of the seven categories of 3D printing.[6] Fused Filament Fabrication (FFF/FDM), a material extrusion process, has been used for SF manufacturing of electrodes. However, some solvent is still required for the mixing stage.[1] A completely solvent-free 3DP is challenging, and to the best of our knowledge only the recent work conducted by our team has achieved this as a proof of concept thus far.[7] The main steps of this process are depicted in Fig 1b. Here AM, CA and two
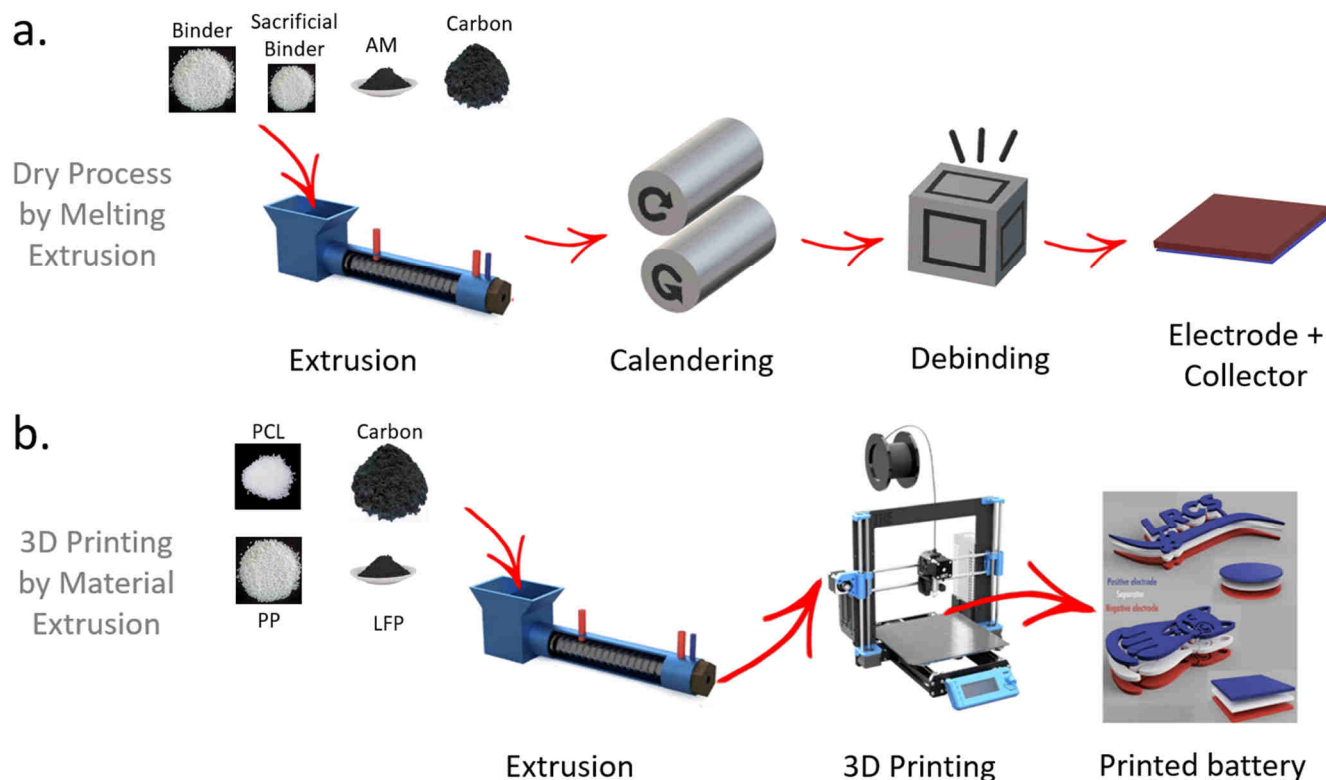
Figure 1. Pathways of solvent-free LIB electrode manufacturing that employ extrusion: a. dry process by melting extrusion (MeltE) and b. 3D printing by material extrusion (3DP).

polymers feed the TSE. The key difference is that both polymers are fundamental components of the final electrode microstructure, therefore there is no debinding step. Polypropylene (PP) acts as a binder giving mechanical stability to the electrode, while polycaprolactone (PCL) provides the electrolyte path after soaking with liquid electrolyte. The resulting filament is fed into the 3D printer allowing for the creation of arbitrary shapes of electrodes. All of the above highlights the key importance of the extrusion step in SF electrode manufacturing. As a relatively new application in the battery field, the extrusion process still holds considerable untapped potential for improvement and optimization. To this end, numerical modeling emerges as an exceptionally promising tool. It offers the opportunity to gain a deeper understanding of the extrusion process and explore various avenues for enhancing its efficiency.

Numerical modeling of single polymer extrusion has extensively been applied in other fields; recent reviews can be found in [8] and [9]. Basically, the process can be divided in three stages: solid transport, melting and liquid flow. The Discrete Element Method (DEM) is commonly employed for studying the particle-particle and particle-extruder interactions during the first stage.[10][11][12] For the second and third stages, continuous approaches, like Computational Fluid Dynamics (CFD) or Smoothed Particle Hydrodynamics (SPH), are more suitable. Recently, Celik et al. [13] proposed an approach coupling DEM and CFD, that allows the study of the three extrusion stages. This approach which presents a high computational cost has not yet been applied to real extruder geometries. The challenge is even greater when modeling the extrusion of dense suspensions, such as those encountered in SF battery electrode manufacturing. This is because in this process, the AM and CA do not melt but are

present in high concentrations within the paste. A similar fluid-solid interaction in twin-screw domains arises in other applications such as wet granulation and wet mixing. Washino et al. [14] proposed a CFD-DEM model of wet granulation in a small domain of a mixer. Computational cost can be reduced by implicitly considering the fluid effect on the particles by using a hydrodynamic force. This approach was employed for the simulation of a section of a twin-screw granulator [15] and for the modeling of a dense suspension extrusion in a square-entry die.[16] This methodology ensures a robust representation of the fluid influence; however, this fluid phase is not part of the obtained microstructure.

On the other hand, in the slurry casting process, Coarse Grained Molecular Dynamics and DEM methods developed by our research group were able to represent explicitly a liquid phase during slurry,[17] drying [18] and to calibrate their parameters with experimental viscosities and densities.[19] The same methods were applied by our group for the simulation of the calendering process.[20] These are mesostructural approaches, yet, the term microstructural is employed hereafter, as commonly used in the battery field. By considering explicitly the AM solid particles and the other particles, DEM allows to study mixing and aggregation among all the materials. The influence of the dispersion of carbon black was analyzed experimentally and numerically for a small amount of particles.[21] Srivastava et al. [22] related the cohesion and adhesion at the mesostructure with the electrochemical and mechanical properties of the electrode. Finally, Ludwig et al. [23] investigated the scenarios of dry mixing (carbon, binder and active material) for different values of cohesion among the particles in a simple geometry. Finally, for the slurry process, a model was proposed to investigate the behavior of a viscous fluid

2

(high solid content) in a section of a TSE using SPH.[24] This model, using real slurry rheological data, allows to calculate local shear rates, however a microstructure cannot be obtained due to its continuum nature.

To the best of our knowledge, the modeling of the extrusion process for the dry manufacturing of electrodes has never been reported before. The present study proposes a new microstructural DEM model of extrusion during SF battery electrode manufacturing. The solid and molten phases are explicitly considered in the entire geometry of a twin-screw extruder. The simplifications made regarding the molten phase allow to simulate hundreds of thousands of particles, which yield representative electrode microstructures.

In the following we start by describing the characteristics and assumptions of our model. Subsequently, we investigate different feeding approaches, cohesion levels and extruder rotation speeds. The obtained electrode microstructures, using a realistic experimental formulation, are critically analyzed. Finally, we conclude and indicate further directions for our work.

Model

Our model is intended to describe the extrusion step of both SF processes that are shown in Fig. 1. The following description is focused in the 3DP process (Fig. 1b) due to the availability of the required experimental apparatus in our facilities. The raw materials used in our experiments are the active material LiFePO$_4$ (LFP), carbon nanofibers, the polymeric binder PP and PCL the polymer for the electrolyte path. For simplicity, and to focus on the electrode microstructure, the PCL is not considered in this study. Our SEM images of the extruded filament show complex networks among PP, carbon nanofibers and LFP (see Fig. S1 in SI). For simplicity in this first model, we assume two distinct particle types, one for the AM and another, labeled BC (Binder-Carbon), which is composed of PP and carbon nanofibers, as shown in Fig. 2. Our model is based on the classical DEM,[25] where particles are represented as spheres. The extrusion simulation is carried out in a generic conical twin-screw extruder, adapted from [26], the same type as our laboratory extruder. The particle size distribution of LFP (Fig. S2 of SI) ranges from 0.3 µm to agglomerates of 20 µm. Assuming 10 µm LFP agglomerate particles, filling the extruder completely would require around 10^9 particles, which is unfeasible for DEM simulations with reasonable computational cost. Neglecting fluid coupling, using periodic boundary conditions and the scaling of the particles are the main solutions for reducing the computational cost.[27] The former is already assumed, while the second one is avoided due to the absence of guaranteed periodic flow in the current extruder setup. Therefore, we opt for a change of scale of the extruder as a means of reducing computational cost. The outlet is reduced from its experimental diameter of 2000 µm to 60 µm (Fig. 2). According to our preliminary tests, any further decrease in the extruder size causes a change in the particle dynamics due to the accumulation of the particles in the inter-screw region. The BC particles are assumed to have a lower size than the AM particles so that they are able to form a continuous phase. However, very low values significantly

increase the computational time, as a compromise, 5 µm is the selected diameter. The impact of lower diameter particles will be investigated in future work.

In our extrusion simulation, the particles are subjected to gravity, particle-particle and particle-wall interactions. Two types of interactions are identified: a repulsive force due to collisions and an attractive force caused by cohesion. Regarding the latter, we neglect noncontact forces (Lennard-Jones and van der Waals) for simplicity. The cohesion force (F_C) for particles in contact is given by the Simplified JKR model:

$$F_C = -c_{CED} A \, n \tag{1}$$

where c_{CED} is the contact energy density, A the contact area and n the unit normal vector. The normal (F_E^n) and tangential (F_E^t) collision forces are calculated with the elastic Hertzian model:

$$F_E^n = k_n \delta^{3/2} \, n - \gamma_n \delta^{1/4} v_r^n \tag{2}$$

$$F_E^t = -min\left(\mu_t |F_E^n|, \left| -k_t \delta^{1/2} S_t - \gamma_t \delta^{1/4} v_r^t \right| \right) t \tag{3}$$

where δ is the overlap distance, v_r^n and v_r^t the normal and tangential relative velocities, μ_t the friction coefficient, S_t the accumulated tangential displacement and t the unit tangential vector. The remaining constants are given by the following expressions depending on the effective material parameters E_{ef} Young's modulus, Shear modulus G_{ef} (depending on the Poisson ratio Po), restitution coefficient and the effective radius of the two particles in contact: $k_n = \frac{4}{3} E_{ef} \sqrt{R_{ef}}$, $\gamma_n = \frac{2\sqrt{5}}{\sqrt{6}} \frac{\ln e}{\sqrt{\ln^2 e + \pi^2}} \sqrt{2 E_{ef} m_{ef}} \sqrt[4]{R_{ef}}$, $k_t = 8 G_{ef} \sqrt{R_{ef}}$ and $\gamma_t = \frac{2\sqrt{5}}{\sqrt{6}} \frac{\ln e}{\sqrt{\ln^2 e + \pi^2}} \sqrt{8 G_{ef} m_{ef}} \sqrt[4]{R_{ef}}$. In order to give a more fluid-like solid behavior for the BC particles, low Young's and high Poisson ratio are defined for this particle type. Experimental measurements show that PP has a very high viscosity (800 Pa.s) during the extrusion (Fig. S3 in SI). In addition, solid carbon nanofibers are part of the BC particle. All this mitigates the inaccuracy of representing this phase as a solid. The cohesion parameter value is chosen to achieve a dense suspension flow, which is assessed by visual inspection of the trajectories. The impact of this value is investigated in the next section. A calibration of these values with experimental data is needed in future work. Rolling friction is also considered by employing the constant directional torque (CDT) model.

The Young's Modulus and the Poisson ratio of LFP is found in literature.[28] Using these parameters, the Rayleigh time step can be estimated. The immediate choice of a timestep equal to 20 % of Rayleigh time, as suggested in literature, results in a very long simulation time for filling the extruder. Higher timesteps yielded numerical instability in the simulations. Therefore, a decrease in 3 orders of magnitude of LFP Young's modulus is necessary in order achieve feasible running times and stability. A similar reduction changed the quantitative results for DEM simulations of cohesionless particles but not the trend,[29] which is the essential
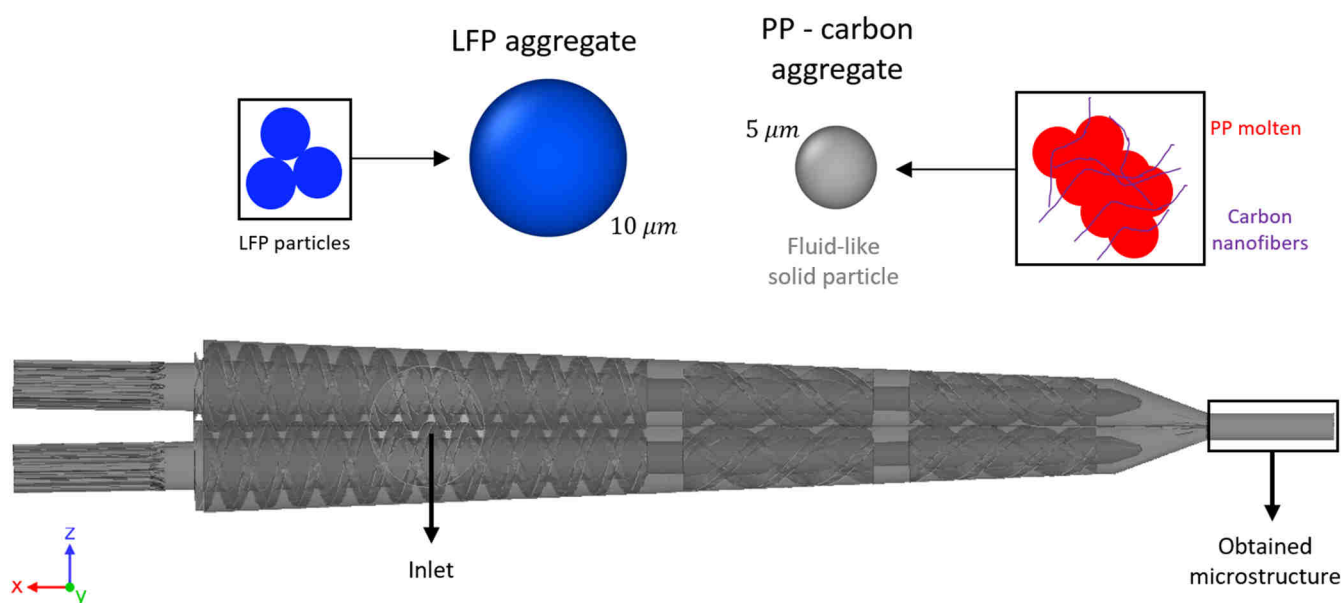
3

Figure 2. Schematic of the particles and extruder considered in this work.

for our comparative analysis in this work. The same decrease was applied on the Young's modulus of all materials to minimize the effect on the real particle dynamics. The values of the model parameters are given in Table S1 of the SI. Our simulations, involving around 200 000 particles, take between 6-15 days depending mainly on the chosen rotation speed of the extruder. We used 64 cores AMD EPYC 7513 @ 2.60GHz (256 GB of RAM) of the MatriCs platform (Université de Picardie-Jules Verne, France). The following open-source software were used: LIGGGHTS [30] for the DEM simulations, OVITO [31] for visualization and MeshLab [32] for modifying the extruder geometry. The commercial software GeoDict (Math2Market)[33] was employed for post-processing.

Results and Discussion

Our proposed model is used for the same formulation than in our extrusion experiments,[7] excluding the PCL polymer, which is not considered here (Table 1). We investigate the influence of the feeding approach, cohesion level and extruder speed on the materials mixing and resulting electrode microstructure. A cylindrical section is added at the extruder outlet (Fig. 2) to mimic the cylindrical filament formed after the solidification of the paste on a conveyor belt downstream from the extruder. In the simulations, the electrode properties are analyzed in the microstructure obtained at the cylindrical section. Except case E, all simulations are carried out at 500 rpm in order to save computational time.

Selection of Feeding Approach

The order in which the materials are fed into the extruder impacts the final product. In our experiments, the polymer powders are fed initially and go through the extruder in a continuous loop by means of a recirculation system. Once the polymers are molten, a premix of LFP and carbon powders is fed into the extruder. We simulate

Table 1. Formulation and density of the components considered in extrusion.

Component	Density (kg/m^3)	Mass fraction	Volume fraction
LFP	3.51	0.65	0.35
PP	0.90	0.28	0.58
Carbon	1.90	0.07	0.07

one passage of the materials until the extruder is filled and a steady-state at outlet is achieved. Therefore, the exact feed conditions of experiments cannot be reproduced. As an alternative, three different strategies are employed and analyzed (Fig 3). Scenario A mimics a premix of LFP and BC, while the others consider the two powders as initially separate. B considers the two powders entering continuously one after the other, while in the feeding approach C, the inlets are located side by side.

The 3D view of the extrusion process (Fig. 3) clearly shows that scenario C has the lower mixing quality. In order to quantify the extent of mixing across the entire extruder, a Radial Distribution Function (RDF) can be estimated (right hand side of Fig. 3). The RDF shows a larger peak at 10 µm corresponding to LFP-LFP contacts, in scenario C, indicating poor mixing. Due to the recirculation system used in our laboratory, this is not observed in our simulations, but it could appear in industrial extruders that commonly have a single passage. In that case, the scenario can be mitigated by a premixing of all the components as reported in at least one laboratory SF process.[5] Scenarios A and B only slightly differ near the inlet region, though they quickly homogenize. Therefore, scenario C is the most critical for mixing quality during the simulated extrusion. This is the one chosen for the investigations in the subsequent sections, since in that case the simulations can provide more interesting information.
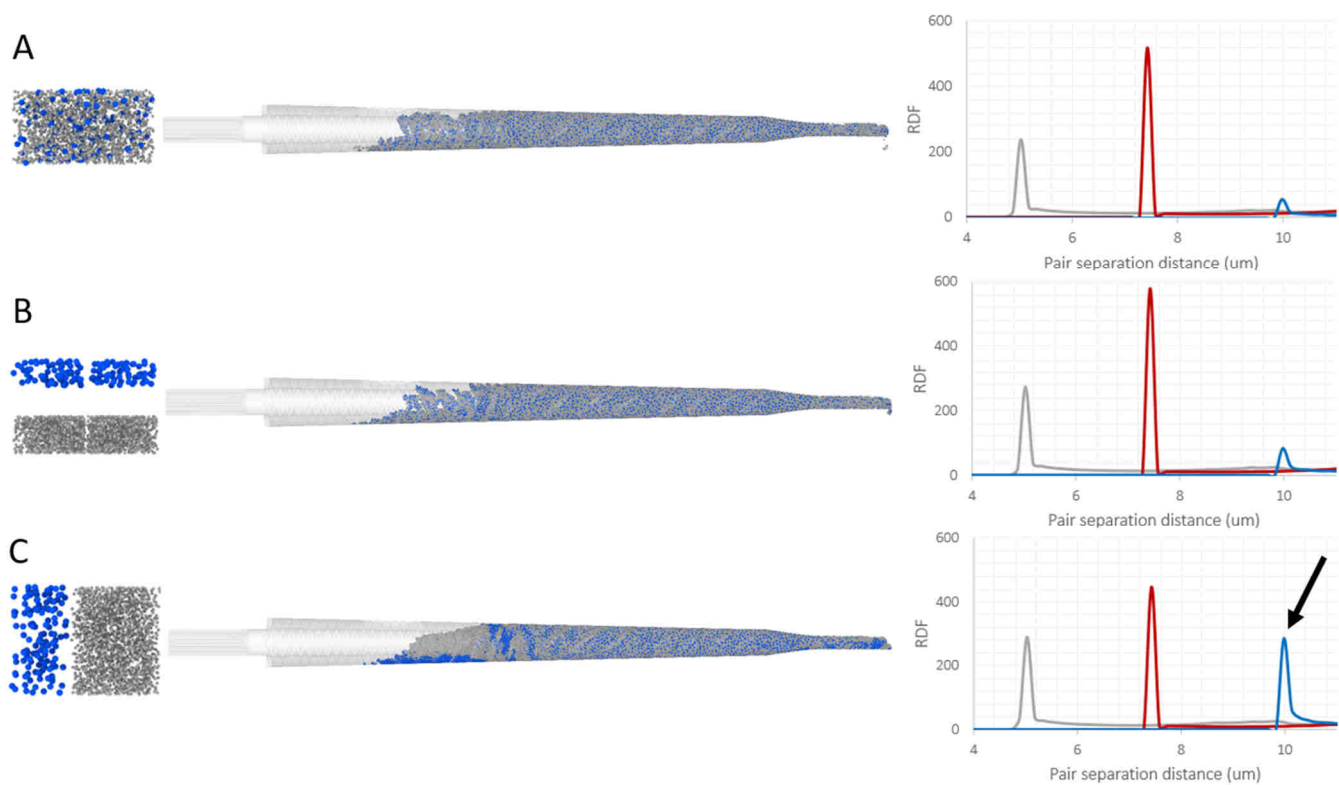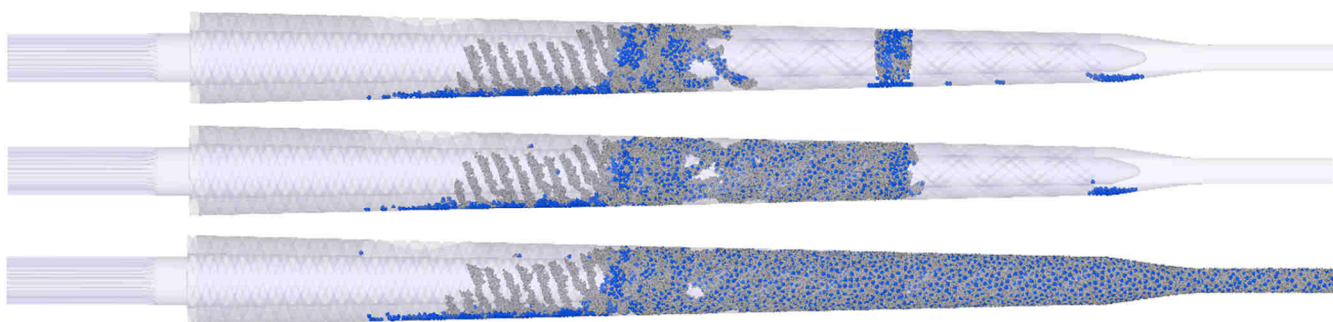
4

Figure 3. Mixing states and radial distribution functions (RDF) for three different feeding approaches. In RDF graphs, BC-BC (grey), BC-AM (red) and AM-AM (blue). The black arrow highlights the larger value of AM-AM contacts for case C.

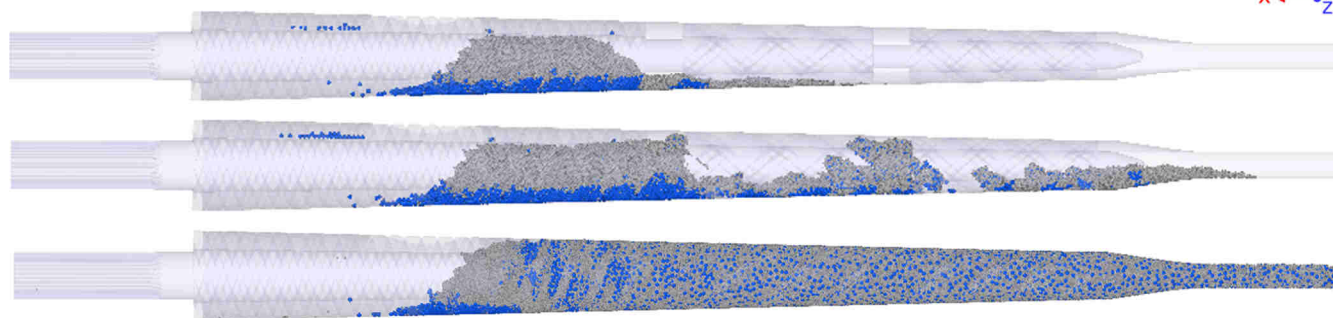## Impact of Cohesion

Case D

Case C

Figure 4. Evolution of extruder filling for a highly cohesive (case D) and low cohesive (case C) pastes.

5

Here the impact of the cohesion strength of LFP-BC and BC-BC on the electrode microstructure is evaluated. In simulations, this is achieved by changing the cohesion energy density (CED) of both interactions. The aim of this comparison is to indirectly elucidate the impact of polymer viscosity, which depends on the chosen extrusion temperature, that is not an obvious decision for experimentalists. Broadly speaking, an increase in viscosity can be represented by an increase in CED. One simulation with lower values of CED (case C) and one with higher values are carried out (case D). The specific CED values are presented in Table S2. Fig 4. shows snapshots of the extruder as if completely fills for both scenarios. As expected, case D exhibits a more compact flow. The difference is expected to accentuate for the case where the extruder has a continuous screw section, as in many real configurations. Furthermore, in the initial stages, the extrusion product shows poor mixing for case C, which is improved as the extruder fills.

Once these two cases with different cohesion were obtained, its impact on the electrode properties can be studied. To calculate the structural parameters of the resulting electrode a similar procedure is used as in our previous publication.[34] The details are specified in the SI section. Due to the difficulty in accurately measuring some of the AM and BC properties, those values are calculated from estimated parameters. While no absolute values are provided, our characterization allows us to compare between simulation cases. The 3D-resolved electrode microstructures for each case are depicted in Fig 5. Case D has higher electrical conductivity (σ_e) mainly because of the lower porosity (ε) that allows the presence of more conductive BC particles. On the other hand, mesostructure C presents a lower tortuosity factor (τ) and a higher effective diffusivity (D_{eff}) which means higher ionic conductivity. This highlights a compromise between electrical and ionic conductivities
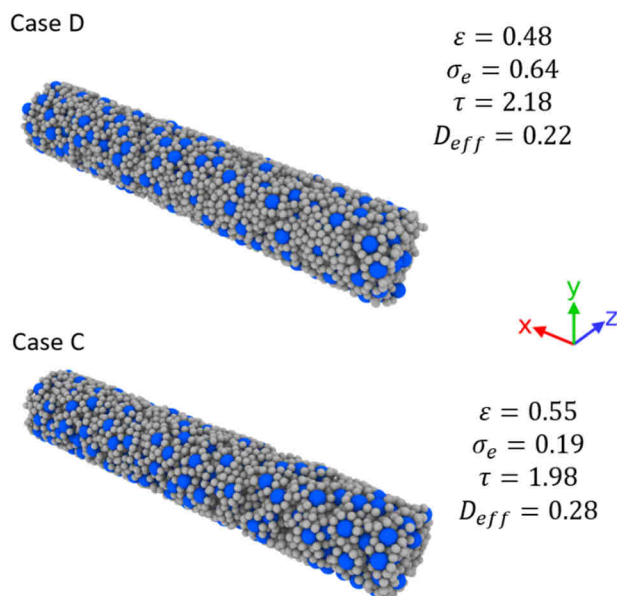
Influence of extruder speed

Our lab experiments are carried out at a screw rotation frequency of 50 rpm. Tests at higher frequencies are planned to investigate its effect on the produced filament. While this extruder allows up to 400 rpm, due to the high viscosity of the paste, maximum feasible experiments should be at around 150 rpm. For industrial applications, extruders should allow higher frequencies. Numerical simulations can contribute to anticipate the effects at very high rotations in a cheaper and safer way. For comparison purposes, here simulations at 50 rpm (case E) and 500 rpm (case C) are carried out.
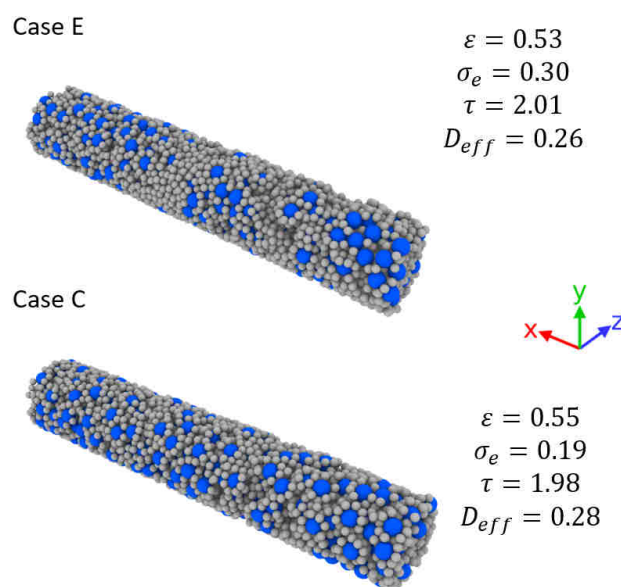

Case E
$$\varepsilon = 0.53$$
$$\sigma_e = 0.30$$
$$\tau = 2.01$$
$$D_{eff} = 0.26$$

Case C
$$\varepsilon = 0.55$$
$$\sigma_e = 0.19$$
$$\tau = 1.98$$
$$D_{eff} = 0.28$$

Figure 6. Microstructures and properties of the obtained electrodes for different extruder rotations speeds: 500 rpm (case E) and 50 rpm (case C).

Fig. 6 shows the obtained 3D electrode microstructures for both cases. The lower speed case resulted in lower porosity, leading to slightly lower ionic conductivity, and higher electrical conductivity. Therefore, there is a compromise when increasing the rotation speed. In experiments, Dreger *et al.* [35] found a compromise during the extrusion step in the wet electrode manufacturing. Increasing rotation speed under a given speed caused an increase of the electrical conductivity. However further increases of speed had the opposite effect. They pointed to the high reduction of the carbon agglomerates size as a cause for the decrease of electrical conductivity at very high speeds. Although, we do not explicitly consider the carbon in the simulation, we can study the agglomeration through our BC particles. To this end, we investigated and removed the AM particles in the obtained microstructures as a post-processing step. Then the coordination number is calculated to provide an idea of the BC-BC agglomeration. Fig. 7 shows lower coordination numbers for the higher speed case. Thus, similar to the experimental observations, simulations confirmed that very high speeds decrease the size of the carbon agglomerates, which results in lower electrical conductivities. On the other hand, the lower speed case shows poor mixing, which can result in some decreasing of its electrical

Case D
$$\varepsilon = 0.48$$
$$\sigma_e = 0.64$$
$$\tau = 2.18$$
$$D_{eff} = 0.22$$

Case C
$$\varepsilon = 0.55$$
$$\sigma_e = 0.19$$
$$\tau = 1.98$$
$$D_{eff} = 0.28$$

Figure 5. Microstructures and properties of the obtained electrodes for a highly cohesive (case D) and low cohesive (case C) pastes.

6

conductivity when modeling explicitly the carbon additive in future work.
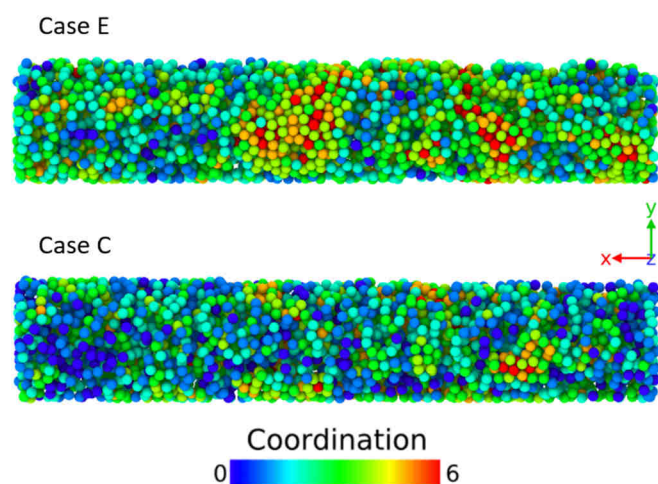

Figure 7. Coordination number of the obtained electrode considering only BC-BC contacts and for different extruder rotations speeds: 50 rpm (case E) and 500 rpm (case C).

Conclusion

A 3D microstructural proof of concept model of extrusion during solvent-free LIB electrode manufacturing is proposed. Active material particles and an equivalent particle consisting of binder and carbon additive were considered. In this respect, some experimental studies with carbon black as well as our SEM images with carbon nanofibers suggest that an explicit consideration of carbon nanofibers in the simulations will improve in future work the description of the carbon additive mixing in extrusion.

Although extrusion simulations present high computational cost, our appropriate assumptions make feasible the simulation in the entire geometry of a reduced size extruder. This allows the consideration of the complex trajectories of the particles in the extruder that directly impacts the aggregation/disaggregation phenomena. In this way, despite that a simplistic representation of the molten phase is chosen, the model was able to reproduce pastes with different cohesion level, that experimentally can be obtained by changing the extrusion temperature. Still, a further calibration with experimental data and the inclusion of shear forces are required in future work.

Furthermore, the developed approach was able to produce representative 3D electrode microstructures by extrusion. This feature allowed the study of the influence of the extruder speed on the electrode microstructure. Simulations for very high extruder speeds were able to reproduce the experimental observation of decreased in cathode electrical conductivity due to carbon contact loss. Prediction of increasing conductivities as speed raises at low values, are to be expected with an explicit consideration of carbon additive, following experimental evidence. Moreover, experimental and numerical investigations are called for a better understanding of the PP-C interactions, which still remain unknown, unlike the PVdF-C matrix in slurry casting. We also plan to accelerate computational speeds through innovative numerical methods and the use of machine learning.

Our model can be employed for a deeper understanding of the effect of binder-active material ratio studied in solvent-free experiments[5] or adapted to investigate other types of battery technologies such as sodium ion and solid-state batteries. It brings for the first time a digital solution to assist in the optimization of the dry processing of battery electrodes, towards the reduction of the time to market of these new processing methods.

Supporting Information

The authors have cited additional references within the Supporting Information.[36][37][38][39]

PDF document - description of the Supporting Information material.

Video – simulation case A.

Video – simulation case B.

Video – simulation case C.

Video – simulation case D.

Video – simulation case E.

Video - trajectory in the extruder of one AM and one BC particles for case D.

Video – Extruder geometry.

Acknowledgements

[1]   N. Verdier, G. Foran, D. Lepage, A. Prébé, D. Aymé-Perrot, M. Dollé, *Polymers (Basel)* **2021**, *13*, 1–26.

[2]   Y. Lu, C. Z. Zhao, H. Yuan, J. K. Hu, J. Q. Huang, Q. Zhang, *Matter* **2022**, *5*, 876–898.

[3] K. Astafyeva, C. Dousset, Y. Bureau, S. L. Stalmach, B. Dufour, *Batter Supercaps* **2020**, *3*, 341–343.

[4] S. El Khakani, N. Verdier, D. Lepage, A. Prébé, D. Aymé-Perrot, D. Rochefort, M. Dollé, *J Power Sources* **2020**, *454*, DOI 10.1016/j.jpowsour.2020.227884.

[5] C. de la Torre-Gamarra, M. E. Sotomayor, J. Y. Sanchez, B. Levenfeld, A. Várez, B. Laïk, J. P. Pereira-Ramos, *J Power Sources* **2020**, *458*, DOI 10.1016/j.jpowsour.2020.228033.

[6] A. S. T. M. Standard, *Standard Terminology for Additive Manufacturing Technologies*, **2012**.

[7] *[In preparation]* V. Boudeville, S. Grugeon, A. Maurel, M. Louati, S. Panier, A. Cayla, R. Lesieur, S. Ursescu, L. Dupont, *July* **2023**.

[8] M. Hyvärinen, R. Jabeen, T. Kärki, *Polymers (Basel)* **2020**, *12*, DOI 10.3390/polym12061306.

[9] A. Lewandowski, K. Wilczyński, *Polymers (Basel)* **2022**, *14*, DOI 10.3390/polym14020274.

[10] P. A. Moysey, M. R. Thompson, *Polym Eng Sci* **2008**, *48*, 62–73.

[11] J. Trippe, V. Schöppner, *International Polymer Processing* **2018**, *33*, 486–496.

[12] O. Celik, C. Bonten, in *AIP Conf Proc*, American Institute Of Physics Inc., **2016**.

[13] A. Celik, C. Bonten, R. Togni, C. Kloss, C. Goniva, **2021**, DOI 10.3390/polym.

[14] K. Washino, H. S. Tan, M. J. Hounslow, A. D. Salman, *Chem Eng Sci* **2013**, *93*, 197–205.

[15] A. Kumar, S. Radl, K. V. Gernaey, T. De Beer, I. Nopens, *Pharmaceutics* **2021**, *13*, DOI 10.3390/pharmaceutics13070928.

[16] C. Ness, J. Y. Ooi, J. Sun, M. Marigo, P. McGuire, H. Xu, H. Stitt, *AIChE Journal* **2017**, *63*, 3069–3082.

[17] J. Xu, A. C. Ngandjong, C. Liu, F. M. Zanotto, O. Arcelus, A. Demortière, A. A. Franco, *J Power Sources* **2023**, *554*, DOI 10.1016/j.jpowsour.2022.232294.

[18] T. Lombardo, A. C. Ngandjong, A. Belhcen, A. A. Franco, *Energy Storage Mater* **2021**, *43*, 337–347.

[19] T. Lombardo, J. B. Hoock, E. N. Primo, A. C. Ngandjong, M. Duquesnoy, A. A. Franco, *Batter Supercaps* **2020**, *3*, 721–730.

[20] A. C. Ngandjong, T. Lombardo, E. N. Primo, M. Chouchane, A. Shodiev, O. Arcelus, A. A. Franco, *J Power Sources* **2021**, *485*, DOI 10.1016/j.jpowsour.2020.229320.

[21] J. K. Mayer, L. Almar, E. Asylbekov, W. Haselrieder, A. Kwade, A. Weber, H. Nirschl, *Energy Technology* **2020**, *8*, DOI 10.1002/ente.201900161.

[22] I. Srivastava, D. S. Bolintineanu, J. B. Lechman, S. A. Roberts, *ACS Appl Mater Interfaces* **2020**, *12*, 34919–34930.

[23] B. Ludwig, J. Liu, Y. Liu, Z. Zheng, Y. Wang, H. Pan, *J Micro Nanomanuf* **2017**, *5*, DOI 10.1115/1.4037769.

[24] J. F. Meza Gonzalez, H. Nirschl, *Energy Technology* **2023**, DOI 10.1002/ente.202201517.

[25] P. A. Cundall, O. D. L. Strack, *Géotechnique* **1979**, 47–65.

[26] Grabcad, "https://grabcad.com/library/conical-twin-screw-small-size-for-lab-or-prototyping-plastic-extrusion-1," **2023**.

[27] J. P. Morrissey, K. J. Hanley, J. Y. Ooi, *Pharmaceutics* **2021**, *13*, DOI 10.3390/pharmaceutics13122136.

[28] T. Maxisch, G. Ceder, *Phys Rev B Condens Matter Mater Phys* **2006**, *73*, DOI 10.1103/PhysRevB.73.174112.

[29] S. Lommen, D. Schott, G. Lodewijks, *Particuology* **2014**, *12*, 107–112.

[30] C. Kloss, C. Goniva, A. Hager, S. Amberger, S. Pirker, *Progress in Computational Fluid Dynamics* **2012**, *12*, 140–152.

[31] A. Stukowski, *Model Simul Mat Sci Eng* **2010**, *18*, DOI 10.1088/0965-0393/18/1/015012.

[32] P. Cignoni, M. Callieri, M. Corsini, M. Dellepiane, F. Ganovelli, G. Ranzuglia, *MeshLab: An Open-Source Mesh Processing Tool*, **n.d.**

[33] Math2Market GmbH, **2023**.

[34] T. Lombardo, F. Lambert, R. Russo, F. M. Zanotto, C. Frayret, G. Toussaint, P. Stevens, M. Becuwe, A. A. Franco, *Batter Supercaps* **2022**, *5*, DOI 10.1002/batt.202200116.

[35] H. Dreger, W. Haselrieder, A. Kwade, *J Energy Storage* **2019**, *21*, 231–240.

[36] Iron Boar Labs Ltd., "https://www.makeitfrom.com/material-properties/EN-1.4122-X39CrMo17-1-Stainless-Steel," **2023**.

[37] C. Sangrós Giménez, L. Helmers, C. Schilde, A. Diener, A. Kwade, *Chem Eng Technol* **2020**, *43*, 819–829.

[38] A. Shodiev, E. N. Primo, M. Chouchane, T. Lombardo, A. C. Ngandjong, A. Rucci, A. A. Franco, *J Power Sources* **2020**, *454*, DOI 10.1016/j.jpowsour.2020.227871.

[39] R. B. MacMullin, G. A. Muccini, *AIChE Journal* **1956**, *2*, 393–403.